THE JOURNAL OF PHYSICAL CHEMISTRY C

Article

Cite This: J. Phys. Chem. C 2019, 123, 15412−15418

pubs.acs.org/JPCC

A New sp^2−sp^3-Hybridized Metallic Carbon Network for Lithium-Ion Battery Anode with Enhanced Safety and Lithium-Ion Diffusion Rate

Dong Fan,[†] Andrey A. Golov,[‡,§] Artem A. Kabanov,[‡,§] Chengke Chen,[†] Shaohua Lu,[†] Xiao Li,[†] Meiyan Jiang,[†] and Xiaojun Hu*,[†]

[†]College of Materials Science and Engineering, Zhejiang University of Technology, 310014 Hangzhou, China

[‡]Samara Center for Theoretical Materials Science (SCTMS), Samara University, 443011 Samara, Russia

[§]Samara Center for Theoretical Materials Science (SCTMS), Samara State Technical University, 443100 Samara, Russia

Supporting Information

ABSTRACT: Carbon-based materials play a significant role in the development of the next-generation lithium-ion battery technologies. However, the commercial use of anodes has been obstructed by their volume expansion and poor rate performance during the lithiation/delithiation process. Here, by means of first-principles calculations, we identify two hitherto unreported sp^2−sp^3-hybridized carbon allotropes, D_{10} and D_{14} carbon, with space groups *Pmma* and *Pmm*2, respectively. Interestingly, D_{14} carbon is predicted to be metallic with high electron density near the Fermi level. We then demonstrate that this metallic D_{14} carbon is a possible anode material in lithium-ion batteries: it is found that the energy barrier along the two inequivalent migration paths in D_{14} carbon is 0.38 (2.28) eV, which is lower than that of the recently reported bco-C_{16} structure with energy barriers of 0.53 (2.32) eV. Moreover, benefiting from the existence of sp^3-hybridized network in D_{14} carbon, during the process of charging/discharging, Li diffusion routes are robust against the mechanical deformation. Therefore, as compared to graphite, this D_{14} anode show many advantages in lithium-ion battery applications, such as lower Li diffusion barrier, moderate theoretical capacity (319 mA h g^{-1}), lower average open circuit (0.53−0.20 V), and enhanced safety features (only 3.6% volume expansion with full Li insertion).

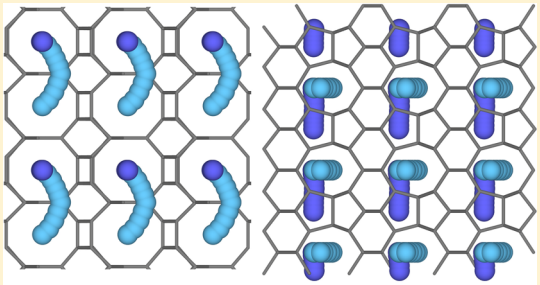

Li diffusion pathways along the Path 1 ( ) and Path 2 ( )

INTRODUCTION

With the growing demand for advanced electronic devices and energy sources, the performance of present lithium-ion batteries (LIBs) needs to be significantly improved.[1,2] Except the electrolyte and cathode, as one of the most important parts in LIBs, various anodes have been extensively identified for better performance, such as lithium (Li) metal,[3] silicon,[4] tin and tin-based intermetallics, and so on.[5] However, these anodes suffer from dramatic volume expansion when alloying with Li (i.e., 400% volume expansion during lithiation of silicon),[6] which will cause pulverization and fracture of the anodes and seriously deteriorate the cycle performance.[7] Therefore, the most generally used anode for commercial LIBs is graphite because of its abundant material supply, long cycle life, and relatively low cost.[7] Unfortunately, during the lithiation process, graphite anode also has been shown to have significant safety issue: the overpotential will lead to Li metal plating on the electrode, which is highly detrimental to the performance of the battery.[8,9] Although volume expansion of anodes can be alleviated by dispersing nanosized particles,[10,11] on account of the large surface area, the volumetric energy density will be greatly reduced and a lot of solid electrolyte interphase will be formed during electrochemical cycling. Therefore, the discovery of a novel bulk material with small volume expansion and good electronic conductivity is a good choice for LIB anode materials.

To this aim, many approaches have been taken to developing high-performance carbon-based anode materials because of its advantages of low-cost, environmentally friendly, and lightweight properties.[12] In addition to graphite, various elusive carbon allotropic modifications have been reported, such as bct-C_8[13] (**atn** topology), bct-C_{40},[14] and T-carbon[15] (**dia-a**). Among all these allotropes, metallic carbon has attracted great attention in recent years for its desirable physical properties and a wide number of applications in superconductivity, catalysis, and electronic devices.[16,17] Over the past decades, around 40 hypothetical metallic allotropes have been reported according to SACADA database,[18] starting from fcc carbon[19] (**fcu**) reported back in 1958. Various other metallic allotropes have been proposed, including $ThSi_2$-type[20] (**ths**), hexagonal H-6[21] (**bto**), K_6 carbon,[22] H_{18} carbon,[23] O- and T-type carbon,[24] C_5 carbon,[25] and K_4 carbon[26,27] (**srs**); however, the K_4 structure is dynamically unstable.[28] Therefore, more efforts are required to design the potential metallic

Received: March 3, 2019
Revised: May 9, 2019
Published: June 3, 2019

DOI: 10.1021/acs.jpcc.9b02034
J. Phys. Chem. C 2019, 123, 15412−15418

carbon allotropes with high thermodynamic stability for experimental preparation.

For LIBs, porous carbon is a potential candidate material because of their porous structure with a plurality of storage sites for Li ions.[29,30] Recently, theoretical computations demonstrated by Liu et al.[31] have predicted that bco-C_{16}, a porous topological semimetal carbon consisting of full sp^2-hybridized carbon atoms, could be a promising anode material for LIBs. However, the diffusion barrier of Li in bco-C_{16} (0.53 eV) is still higher than that of graphite (0.22−0.4 eV), and the volume expansion of fully lithiated bco-C_{16} is 13.4%, which is also higher than that of graphite (10%).[31] Thus, motivated by these considerations, we wonder if we can design a sp^2−sp^3-hybridized carbon allotrope with enhanced safety as well as the metallic feature to avoid the problems discussed above.

In this work, by introducing an interlayer sp^2-hybrid carbon atoms in our recently reported all sp^3-bonded D-carbon structure,[32] we report the design of a new three-dimensional orthorhombic carbon phase in *Pmma* (*Pmm*2) symmetry with 10 (14) atoms in one primitive cell, thus termed D_{10} (D_{14}) carbon hereafter. These two hitherto unreported structures are dynamically and thermally stable and with a mass density of 2.51−2.76 g cm^{-3}. D_{10} carbon is a semiconductor with an indirect gap of 1.82 eV, whereas D_{14} carbon possesses metallic properties. Because of the novel metallic property of the D_{14} structure, we mainly focused our attention on the D_{14} carbon to investigate its potential application. Considering the porous feature of D_{14}, the Li storage and migration capabilities are discussed. The calculated diffusion barrier is lower than that of graphite, indicating a higher Li-ion diffusion rate. Importantly, because of the existence of sp^3-bonded networks, the total volume expansion of D_{14} is only 3.6%, which is obviously lower than that of graphite (10%) and bco-C_{16} (13.4%).[7,31] Therefore, D_{14} promises a higher Li-ion diffusion rate as well as better safety than graphite and bco-C_{16} anodes. Once synthesized, the D_{14} structure would be a promising candidate in the applications of carbon-based energy storage and electronics.

■ COMPUTATIONAL DETAILS

All calculations are performed by utilizing the density-functional theory (DFT) within the general gradient approximation[33] as implemented in the Vienna *Ab initio* Simulation Package (VASP).[34] The electronic exchange−correlation interaction is incorporated by using Perdew−Burke−Ernzerhof (PBE) functional.[33] The Heyd−Scuseria−Ernzerhof hybrid functional (HSE06)[35] is also used for the high accurate band structure calculations. The cutoff energy for wave function is set to 650 eV.[36,37] The convergence thresholds are set to 10^{-5} eV and 10^{-3} eV/Å for total energy and force, respectively. A 9 × 3 × 6 (5 × 5 × 6) Monkhorst−Pack *k*-point mesh is used to represent the reciprocal space of the D_{10} (D_{14}).

Phonon calculations are performed by using the Phonopy package.[38] The diffusion barrier for Li atom is calculated on the basis of the climbing-image nudge elastic band (CI-NEB) method[39] as implemented in the VASP code. The convergence criterion of force is set to be 0.02 eV/Å. *Ab initio* molecular dynamics (AIMD) simulations were performed in an *NVT* ensemble using the Nosé−Hoover method,[40] as implemented in the VASP code within the PBE functional. The time step is set to 1 fs, and the total simulation time is 10 ps. The natural tiling analysis[41] was carried out by means of ToposPro[42] and Systre[43] software. Recently, the natural tiling approach was successfully introduced in the field of carbon allotropes for searching for structural similarity.[44] Also, the natural tiling analysis can be applied for the searching of possible migration channels in solids.[45] More details on computational methods can be found in the Supporting Information.

■ RESULTS AND DISCUSSION

As shown in Figure 1, the D_{14} primitive cell can be described as a new allotrope constructed from 2 × 1 × 1 D-carbon[32] cell

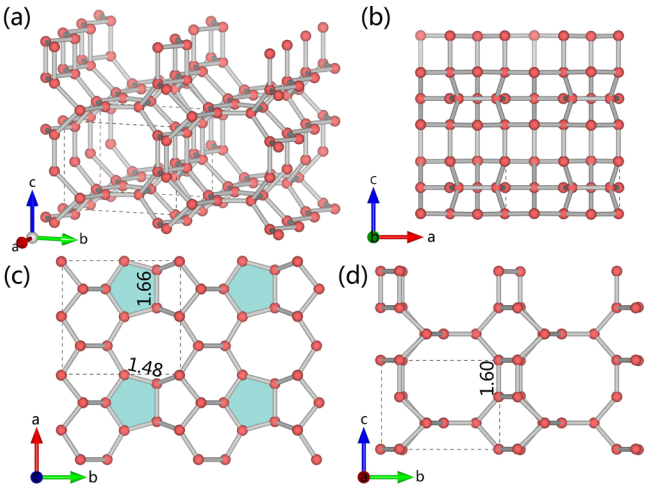

Figure 1. (a) Perspective view of the D_{14} carbon structure. (b−d) Top and side views of the crystal structure of D_{14} carbon. The different C−C bond lengths (Å) are also displayed. The unit cell is characterized by the dash line. Silvery sticks indicate the carbon bonds.

that is inserted by foreign two sp^2-hybridized carbon atoms; D_{10} carbon allotrope is constructed from a D-carbon by inserting the sp^2-bonded carbon atoms between adjacent sp^3-bonded carbon atoms (see Figure S1). The natural tiling of D_{10} allotrope consists of two types of tiles: 6^4 corresponding to the adamantane-like cage of the diamond structure and $4^2.6^4.16^2$, which did not occur in any known-to-us carbon phase (Figure S2). The tiles formed the framework in 1:1 ratio. As shown in Figure 2a−d, the structure of D_{14} is more complicated from the topological point of view than that of D_{10} (Figure S2). The framework assembled from six tiles: [$5^2.6^2$], [6^4], [$6^2.8^2$], [$4^2.6^2.10^2$], [$4^2.5^4.10^2$], and [$4^2.8^2.10^2$] in ratio 1:2:1:2:1:1. The first four tiles have been found in previously proposed carbon allotropes while the last two are novel.

The structural parameters, including the equilibrium density, equilibrium volume, and bulk modulus, are listed in Tables S1 and S2. For D_{10} carbon, we find that the shortest bonds identified with sp^2-hybridized bonds show clear features of the C=C bonds, and the bond lengths between sp^3-hybridized atoms (1.60 Å) are close to those in diamond (1.54 Å), showing features of stretched C−C σ bonds. For D_{14} carbon, the length of the distorted C−C σ bond (1.66 Å, see colored pentagon-shaped region in Figure 1c) is distinctly longer than that of diamond but shorter than that of the previously reported longest C−C σ bond in the reconstructed diamond surface (1.788 Å).[48]

Total energy calculations are implemented to investigate the energetic stability of D_{10} and D_{14} structures. Figure 3a shows the total energy versus volume curves for D_{10} and D_{14}.

DOI: 10.1021/acs.jpcc.9b02034
J. Phys. Chem. C 2019, 123, 15412−15418

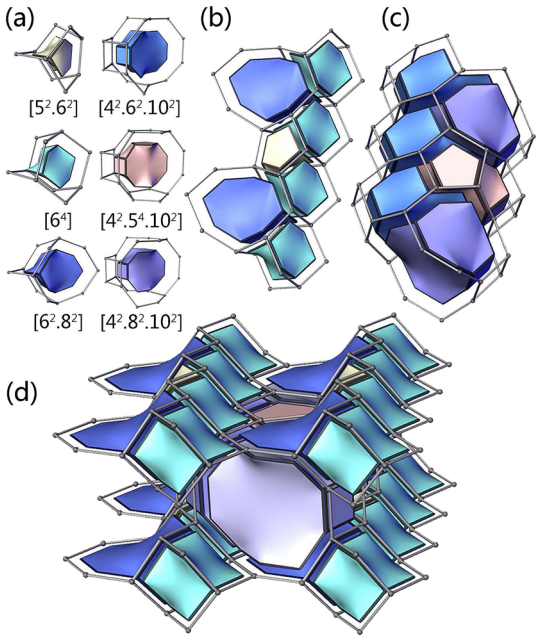

Figure 2. (a–d) Tiles, chains, and natural tilings for D_{14} carbon allotrope.

Previously reported bcc C_8,[46] T-carbon,[47] diamond, and graphite are also shown for comparison. Our results agree well with previously reported first-principles calculations that suggest the validity of the method in this work. For D_{10}, it is energetically more favorable than bcc C_8 and T-carbon. The D_{14} carbon is also metastable compared with diamond and graphite, but still more stable than T-carbon[49] and comparable with bcc C_8 structure.[46]

The dynamical stability of D_{10} and D_{14} was confirmed by computing the corresponding phonon dispersion curves, as presented in Figures S3 and 3b, respectively. There is no imaginary phonon mode in the phonon dispersions at the whole Brillouin zone, indicating the dynamical stability of the structures. Moreover, to verify their thermal stability, additional AIMD simulations have been carried out at 300 and 500 K for the large supercell of D_{10} and D_{14}, containing 120 and 168 carbon atoms, respectively (see Figures 3c and S3). For D_{14} structure, its structural integrity was well kept during the AIMD at 800 K (see Figure S4). Thus, because of the high thermal stability, the synthesis of these new allotropes is feasible.

The mechanical stability of the newly proposed carbon allotropes is also examined by calculating their zero-pressure elastic constants. For a stable orthorhombic structure, C_{11}, C_{12}, C_{13}, C_{23}, C_{33}, C_{44}, C_{55}, and C_{66} are independent, and their elastic constants C_{ij} should satisfy the well-known Born criteria[50]

$$\begin{cases} C_{11} > 0,\ C_{11}C_{22} > C_{12}^{2}, \\ C_{44} > 0,\ C_{55} > 0,\ C_{66} > 0, \\ C_{11}C_{22}C_{33} + 2C_{12}C_{13}C_{23} - C_{11}C_{23}^{2} \\ - C_{22}C_{13}^{2} - C_{33}C_{12}^{2} > 0 \end{cases} \quad (1)$$

As listed in Table S2, the calculated elastic constants of D_{10} and D_{14} allotropes satisfy this criterion, suggesting that their structures are mechanically stable. To further establish the experimental connection of D_{10} and D_{14} allotropes, we calculated the X-ray diffraction (XRD) patterns to compare with experimental data in detonation soot samples (Figure S5).[51] Different from graphite (diamond) where the peaks at 22° (44°) are observed, for D_{10}, the peaks at 11°, 23°, 25°, and 42° are clearly visible. Our calculated XRD patterns show that the diffraction peaks of D_{14} satisfactorily match the previously unexplained peak at 23° and 29°, even though the peak at 23° is broad. For the strongest peak at 17° of the D_{14} structure, it does not match any previously known carbon phases, and this characteristic peak can be used to identify the D_{14} structure in experiments.

Figure S6 shows the orbitally resolved band structure of D_{10} and D_{14}, respectively. The D_{10} carbon is a semiconductor featuring an indirect band gap calculated to be 0.85 eV by the PBE functional and 1.82 eV by the HSE06 hybrid functional (see Figure S7). The conduction band minimum (CBM) and

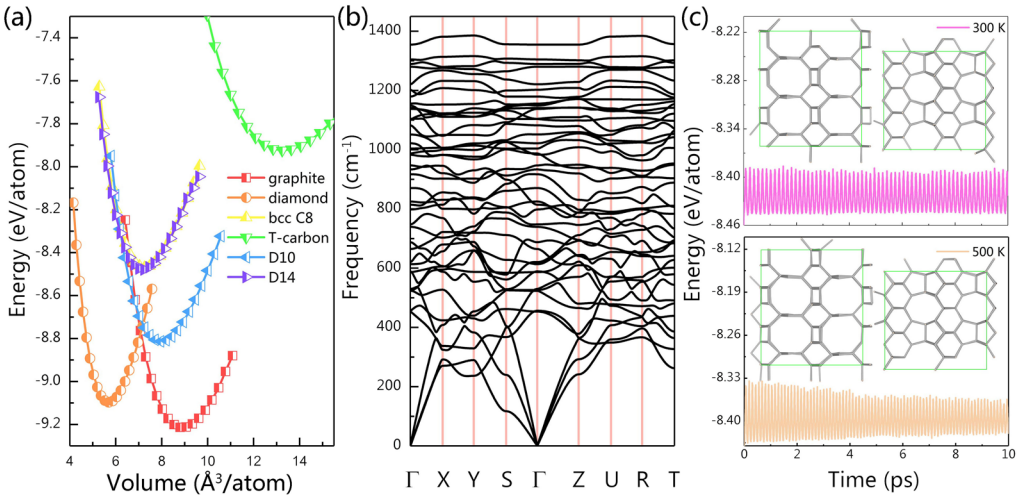

Figure 3. (a) Calculated energy vs volume per atom for D_{14} and D_{10} structures compared to graphite, diamond, bcc C_8,[46] and T-carbon.[47] (b) Calculated phonon dispersion curves of D_{14} structure at zero pressure. (c) Fluctuations of total energy of the D_{14} supercell as a function of the molecular dynamic simulation step with 10 ps at 300 and 500 K. Snapshots of the D_{14} carbon at the end of 10 ps AIMD simulations are also presented.

DOI: 10.1021/acs.jpcc.9b02034
J. Phys. Chem. C 2019, 123, 15412−15418

valence band maximum (VBM) are located at the $Z-U$ and Y point, respectively. Therefore, different from diamond and graphite which are insulator and metallic, the D_{10} carbon is semiconducting with a moderate band gap. The results show that the CBM and VBM of D_{10} are mainly contributed by C_{p_z} states, and there is an obvious orbital hybridization between C_{p_x} and C_{p_z} states below the Fermi level. Interestingly, the D_{14} shows a metallic feature, as the electron density near the Fermi level. To investigate the origin of this metallic feature, we computed the partial density of states (DOS) onto the sp^2- and sp^3-hybridized carbon atoms, as shown in Figure S8, which indicate that the main contribution to the DOS near the Fermi level derives from the p_z orbitals of sp^2-hybridized carbon atoms, and the contribution from the p_z orbitals of sp^3-hybridized is small.

As above-mentioned, semiconducting D_{10} with a high dispersion band structure at CBM suggests a high electron mobility. While for D_{14}, its intrinsic metallic behavior arises from the hybridization of C_{2p} states (see Figure S8). Therefore, is the D_{14} carbon a promising anode for LIBs? To answer this question, we then carried out a comprehensively theoretical investigation on the Li-ion intercalation and diffusion process in D_{14}, by means of first-principles calculations. In the covalent carbon system, van der Waals (vdW) interactions are weak and negligible.[31] Therefore, all results presented in the main text are based on standard PBE functional, unless otherwise stated.

First, we investigated the process of insertion of Li atom(s) into D_{14}. As was shown above, the structure of D_{14} contains six different type of cages according to the natural tiling analysis (Figure 2a). Thus from topological point of view, there are six possible inequivalent Li positions in the structure that correspond to the centers of cages. The binding energy for each of these positions was computed by the DFT method by using the following equation:

$$E_b = \frac{E_{D_{14}Li_x} - E_{D_{14}} - x\mu_{Li}}{x} \quad (2)$$

where $E_{D_{14}Li_x}$ and $E_{D_{14}}$ are the total energies of Li_x inserted D_{14} and pristine D_{14} carbon, respectively. x is the number of inserted Li atoms; μ_{Li} is the chemical potential of Li which is taken as the energy of bulk Li (−1.89 eV per atom, according to our calculations). For the fully Li-intercalated phase, the binding energy E_b is calculated as −0.37 eV, demonstrating that Li atoms can be stably intercalated in D_{14} at sufficiently high Li concentrations.

To gain a more comprehensive perspective on the performance of D_{14} as the anode material, we first search the most stable Li occupying sites (see Figure S9). The insertion of Li atom inside $[5^2.6^2]$ cage leads to significant structural deformation because of the small size of the cage (see Table 1). For large cages ($[6^4]$ and $[6^2.8^2]$), they can adsorb Li without significant volume change theoretically. However, a stable intercalation structure is still difficult to form because of the positive binding energy. Though the cage $[4^2.6^2.10^2]$ has a large enough volume for Li nevertheless during structural optimization, Li moves to the larger neighbor cage $[4^2.8^2.10^2]$ that is more energetically favorable. As expected, two biggest cages $[4^2.5^4.10^2]$ and $[4^2.8^2.10^2]$ are the most suitable for Li intercalation with the values of binding energies equal to −0.495 and −0.660 eV, respectively. These two Li positions form two-dimensional Li-conductivity layers consisting of two types of diffusion paths along a and c directions, as it shown in Figure 4a. The first path goes through the 10-membered ring (see Figure 4b) and have much less activation energy (0.38 eV) than the second one (2.28 eV) passing through the 8-membered ring. We also find that the vdW functional (DFT-D2[52]) give almost the same results (see Figure S10), indicating that vdW interactions in D_{14} carbon are indeed weak. Such a small diffusion barrier is comparable to that of graphite (0.218−0.40 eV)[31] and significantly lower than that of bco-C_{16} (0.53 eV)[31] and the commercially used TiO_2 anode [≈0.6 eV][53]). Thus, D_{14} has predominantly one-dimensional ionic conductivity along the a direction.

Table 1. Binding Energy for Six Unequivalent Positions of Li in the D_{14} Structure[a]

Li position [cage type]	cage volume, (Å^3)	E_b (eV)
no. 1 $[5^2.6^2]$	4.159	–
no. 2 $[6^4]$	5.543	4.693
no. 3 $[6^2.8^2]$	8.316	1.610
no. 4 $[4^2.6^2.10^2]$	16.186	–
no. 5 $[4^2.5^4.10^2]$	20.985	−0.495
no. 6 $[4^2.8^2.10^2]$	24.018	−0.660

[a]"–" means that the relaxation of the structure with the given Li position leads to the structural deformation or significant Li displacement. See the text for more details.

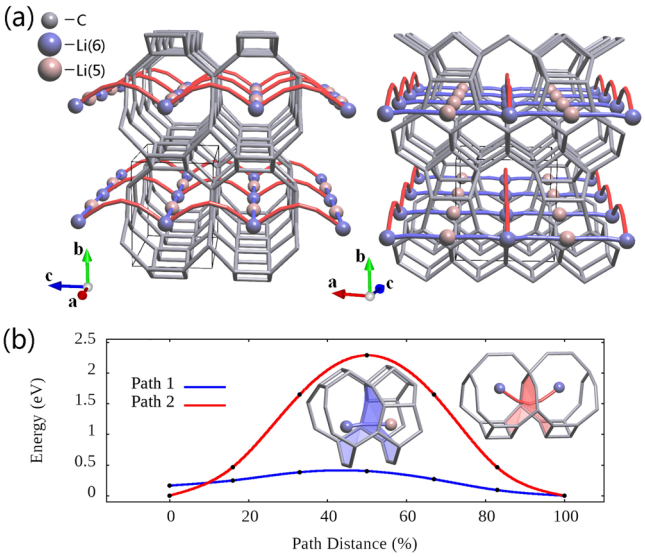

Figure 4. (a) Schematics of the Li diffusion pathways along the path 1 and path 2. (b) Diffusion energy barrier profiles of the two diffusion paths.

Average open circuit voltage (OCV) is another important part which is widely used for evaluating the performance of the LIBs. As it can be seen in Figure 5a, the voltage profile displays a quick drop from 0.53 V when $x \geq 0.375$; then, the voltage profile decreases slowly to 0.26 V with the Li concentration increasing until $x \geq 0.875$. The voltage averaged over $0 < x < 1$ is 0.36 V for Li, which is between those of the commercial anode materials, that is, ∼0.2 V for graphite[54] and 1.5−1.8 V for TiO_2.[55] The low average OCV of D_{14} means that once connected to the cathode, the LIBs can supply a higher operating voltage with larger energy capacity.[31] The potential range of 0.1−1 V is highly desired for an anode material. Therefore, the D_{14} structure can be utilized for high-performance battery applications. Each Li atom loses 0.84|e|

DOI: 10.1021/acs.jpcc.9b02034
J. Phys. Chem. C 2019, 123, 15412−15418

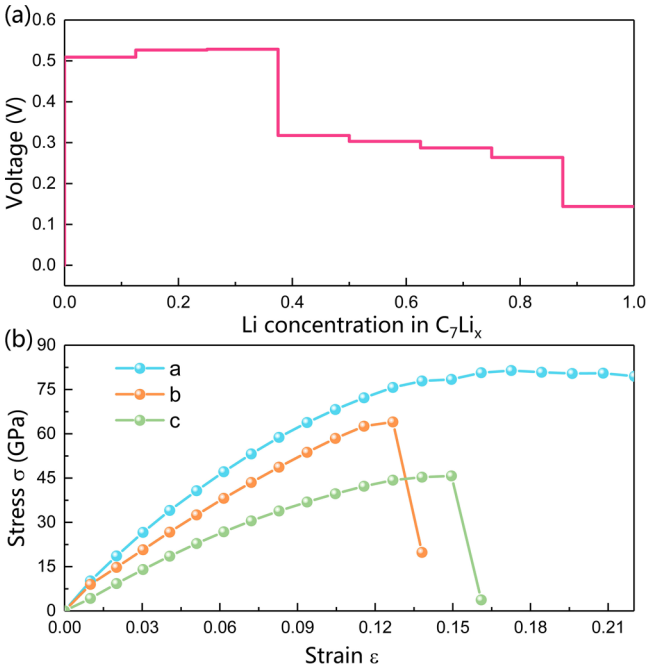

Figure 5. (a) Calculated voltage profile along the minimum energy path. (b) Tensile stress σ as a function of the uniaxial strain along *a*, *b*, and *c* directions, respectively.

based on Bader charge analysis, indicating the ionic feature of the bonding between inserted Li and carbon atoms.

A crucial parameter in evaluating the performance of LIBs, theoretical capacity, can be estimated from the theoretical calculating value, as shown in the Supporting Information. According to our calculations, the theoretical specific capacity of D_{14} is 319 mA h g^{-1}, corresponding to the C_7Li, which is slightly lower than that of graphite, (C_6Li, 372 mA h g^{-1}) but is still about 1.6 times larger than that of the commercial TiO_2 anode (200 mA h g^{-1}).[56] Meanwhile, the DOSs of the $D_{14}Li_x$ during the lithiation process are also investigated because the insertion of Li atoms will lead to the Fermi level shift.[57] As shown in Figure S11, at dilute Li concentrations, the DOS near the Fermi level (ϵ_f) of D_{14} retains its shape, while ϵ_f is shifted to a higher energy. In the energy window around the ϵ_f, Li-inserted D_{14} appears to behave similarly to the electronic dopant (i.e., rigid-band shift). Nevertheless, the effect of Li-inserted D_{14} is not a pure electronic doping because the potential from the Li-atoms also changes the features of the valence states. Although the metallic feature of $D_{14}Li_x$ was maintained during the whole lithiation process, the semi-conducting feature is observed because the adequate Li atoms transfer electrons to the unoccupied C-π states. Therefore, from the electronic conductivity point of view, the corresponding capacity will be reduced to 299 mA h g^{-1}.

During the Li-ion charging/discharging processes, the volume changes will cause the pulverization of electrode crystals, resulting in a poor cycling performance.[58] Therefore, we consider the cycling stability of D_{14} determined by the volume changes with Li insertion. We calculated the volume changes of fully lithiated D_{14} compared with the pristine D_{14}. The calculated results demonstrate that there is no bond breaking or switching occurs, and the total volume expansion is only 3.6%, which is obviously lower than that of graphite (10%) and bco-C_{16} (13.4%)[7,31] because of the existence of sp^3-bonded networks. Therefore, although D_{14} is a metastable phase compared to graphite, D_{14} offers a more secured performance for rechargeable batteries because of the small volume expansion during the Li-ion intercalation process. Moreover, different from graphite and bco-C_{16}, the volume changes of D_{14} are mainly in the *b* direction (1.8%). To further assess the cyclic stability, the stress−strain relations of D_{14} are calculated within uniaxial tensile strain. As shown in Figure 5b, the stresses increase with the increasing strains. Below 13%, there is no abrupt decrease in the stress, indicating that the structure integrity of the D_{14} anode can be maintained even under large strain.

■ CONCLUSIONS

In summary, we designed two hitherto unknown carbon allotropes, D_{10} and D_{14}, composed of mixed sp^2−sp^3 bonding networks. The newly proposed allotropes in this work are energetically more favorable than many previously proposed allotropes. State-of-the-art theoretical calculations demonstrate that these phases are dynamically, mechanically, and thermally stable. Electronic band structure calculations reveal that D_{10} is a semiconductor with a moderate band gap (1.82 eV); whereas D_{14} is predicted to be metallic with a high electron density around the Fermi level. With these remarkable advantages, D_{14} carbon shows a great potential for the use of the all-carbon material as an anode in LIBs. Our results provide not only a perspective for the novel structure of mixed sp^2−sp^3 carbon allotropes but also promote future research to probe new stable allotropic modification of carbon with extraordinary electronic properties for high-performance applications.

■ ASSOCIATED CONTENT

Supporting Information

The Supporting Information is available free of charge on the ACS Publications website at DOI: 10.1021/acs.jpcc.9b02034.

Details of computational methods, elastic constants, and orbital-projected DOS of D_{14} carbon; structural parameters and atomic positions of D_{14} and D_{10} structures; atomic structure, tilings, and phonon dispersion curves of D_{10} carbon; and band structures (PBE and HSE06) of D_{14} and D_{10} carbon (PDF)

■ AUTHOR INFORMATION

Corresponding Author

*E-mail: huxj@zjut.edu.cn.

ORCID

Dong Fan: 0000-0003-1873-3416

Artem A. Kabanov: 0000-0002-3388-6122

Xiaojun Hu: 0000-0001-7851-9900

Notes

The authors declare no competing financial interest.

The structural (vasp) data in this work, and the output of *NVT*-MD simulation results, that support the findings of this study, are available at https://github.com/agrh/Papers. Any other information supporting the conclusions presented is available from the authors upon request.

■ ACKNOWLEDGMENTS

The work was carried out at the National Supercomputer Center in Guangzhou, and the calculations were performed on TianHe-2. Topological/geometrical analysis of cavities and channels as well as Li-diffusion pathways were done within

Russian Science Foundation project no. 16-13-10158. This work was supported by the National Natural Science Foundation of China (grant nos. 11504325, 50972129, and 50602039) and the Natural Science Foundation of Zhejiang Province (LQ15A040004). It was also supported by the Key Project of the National Natural Science Foundation of China (U1809210), the International Science Technology Cooperation Program of China (2014DFR51160), the National Key Research and Development Program of China (2016YFE0133200), and the One Belt and One Road International Cooperation Project from Key Research and Development Program of Zhejiang Province (2018C04021). A.A.K. thanks the Russian Foundation for Basic Research for a partial support with grant #16-32-00296 mol_a and the Russian Ministry of Science and Education for a partial support with grant #3.7626.2017/9.10. The authors gratefully acknowledge the suggestions and advice of Prof. D. M. Proserpio.

■ REFERENCES

(1) Armand, M.; Tarascon, J.-M. Building Better Batteries. *Nature* **2008**, *451*, 652.

(2) Choi, J. W.; Aurbach, D. Promise and Reality of Post-lithium-ion Batteries with High Energy Densities. *Nat. Rev. Mater.* **2016**, *1*, 16013.

(3) Liu, J.; Zhao, T.; Zhang, S.; Wang, Q. A New Metallic Carbon Allotrope with High Stability and Potential for Lithium Ion Battery Anode Material. *Nano Energy* **2017**, *38*, 263−270.

(4) Su, X.; Wu, Q.; Li, J.; Xiao, X.; Lott, A.; Lu, W.; Sheldon, B. W.; Wu, J. Silicon-based Nanomaterials for Lithium-ion Batteries: A Review. *Adv. Energy Mater.* **2014**, *4*, 1300882.

(5) Winter, M.; Besenhard, J. O. Electrochemical Lithiation of Tin and Tin-based Intermetallics and Composites. *Electrochim. Acta* **1999**, *45*, 31−50.

(6) Kasavajjula, U.; Wang, C.; Appleby, A. J. Nano- and Bulk-silicon-based Insertion Anodes for Lithium-ion Secondary Cells. *J. Power Sources* **2007**, *163*, 1003−1039.

(7) Zhang, W.-J. A Review of The Electrochemical Performance of Alloy Anodes for Lithium-ion Batteries. *J. Power Sources* **2011**, *196*, 13−24.

(8) Belharouak, I.; Koenig, G. M., Jr; Amine, K. Electrochemistry and Safety of $Li_4Ti_5O_{12}$ and Graphite Anodes Paired with $LiMn_2O_4$ for Hybrid Electric Vehicle Li-ion Battery Applications. *J. Power Sources* **2011**, *196*, 10344−10350.

(9) Kim, H.; Lim, K.; Yoon, G.; Park, J.-H.; Ku, K.; Lim, H.-D.; Sung, Y.-E.; Kang, K. Exploiting Lithium-Ether Co-Intercalation in Graphite for High-Power Lithium-Ion Batteries. *Adv. Energy Mater.* **2017**, *7*, 1700418.

(10) Magasinski, A.; Dixon, P.; Hertzberg, B.; Kvit, A.; Ayala, J.; Yushin, G. High-performance Lithium-ion Anodes Using A Hierarchical Bottom-up Approach. *Nat. Mater.* **2010**, *9*, 353.

(11) Zhang, W.-M.; Hu, J.-S.; Guo, Y.-G.; Zheng, S.-F.; Zhong, L.-S.; Song, W.-G.; Wan, L.-J. Tin-nanoparticles Encapsulated in Elastic Hollow Carbon Spheres for High-performance Anode Material in Lithium-ion Batteries. *Adv. Mater.* **2008**, *20*, 1160−1165.

(12) Wu, Y. P.; Rahm, E.; Holze, R. Carbon anode materials for lithium ion batteries. *J. Power Sources* **2003**, *114*, 228−236.

(13) Baughman, R. H.; Galvão, D. S. Tubulanes: Carbon Phases Based on Cross-linked Fullerene Tubules. *Chem. Phys. Lett.* **1993**, *211*, 110−118.

(14) Wang, J.-T.; Nie, S.; Weng, H.; Kawazoe, Y.; Chen, C. Topological Nodal-Net Semimetal In A Graphene Network Structure. *Phys. Rev. Lett.* **2018**, *120*, 026402.

(15) Burdett, J. K.; Lee, S. Moments Method and Elemental Structures. *J. Am. Chem. Soc.* **1985**, *107*, 3063−3082.

(16) Terrones, H.; Terrones, M.; Hernández, E.; Grobert, N.; Charlier, J.-C.; Ajayan, P. M. New Metallic Allotropes of Planar and Tubular Carbon. *Phys. Rev. Lett.* **2000**, *84*, 1716.

(17) Ni, Y.; Yao, K.-L.; Fu, H.-H.; Gao, G.-Y.; Zhu, S.-C.; Luo, B.; Wang, S.-L.; Li, R.-X. The Transport Properties and New Device Design: The Case of 6,6,12-graphyne Nanoribbons. *Nanoscale* **2013**, *5*, 4468−4475.

(18) Hoffmann, R.; Kabanov, A. A.; Golov, A. A.; Proserpio, D. M. Homo Citans and Carbon Allotropes: For An Ethics of Citation. *Angew. Chem., Int. Ed.* **2016**, *55*, 10962−10976.

(19) Casella, R. C. Energy-band Structure of A Hypothetical Carbon Metal. *Phys. Rev.* **1958**, *109*, 54.

(20) Hoffmann, R.; Hughbanks, T.; Kertesz, M.; Bird, P. H. Hypothetical Metallic Allotrope of Carbon. *J. Am. Chem. Soc.* **1983**, *105*, 4831−4832.

(21) Tamor, M. A.; Hass, K. C. Hypothetical Superhard Carbon Metal. *J. Mater. Res.* **1990**, *5*, 2273−2276.

(22) Niu, C.-Y.; Wang, X.-Q.; Wang, J.-T. K_6 Carbon: A Metallic Carbon Allotrope in sp^3 Bonding Networks. *J. Chem. Phys.* **2014**, *140*, 054514.

(23) Zhao, C.-X.; Niu, C.-Y.; Qin, Z.-J.; Ren, X. Y.; Wang, J.-T.; Cho, J.-H.; Jia, Y. H18 Carbon: A New Metallic Phase with sp2-sp3 Hybridized Bonding Network. *Sci. Rep.* **2016**, *6*, 21879.

(24) Liu, Y.; Jiang, X.; Fu, J.; Zhao, J. New Metallic Carbon: Three Dimensionally Carbon Allotropes Comprising Ultrathin diamond nanostripes. *Carbon* **2018**, *126*, 601−610.

(25) Wei, Q.; Zhang, Q.; Yan, H.; Zhang, M.; Wei, B. A New Tetragonal Superhard Metallic Carbon Allotrope. *J. Alloys Compd.* **2018**, *769*, 347−352.

(26) O'Keeffe, M.; Adams, G. B.; Sankey, O. F. Predicted New Low Energy Forms of Carbon. *Phys. Rev. Lett.* **1992**, *68*, 2325.

(27) Itoh, M.; Kotani, M.; Naito, H.; Sunada, T.; Kawazoe, Y.; Adschiri, T. New Metallic Carbon Crystal. *Phys. Rev. Lett.* **2009**, *102*, 055703.

(28) Yao, Y.; Tse, J.; Sun, J.; Klug, D.; Martoňák, R.; Iitaka, T. Comment on New Metallic Carbon Crystal. *Phys. Rev. Lett.* **2009**, *102*, 229601.

(29) Goriparti, S.; Miele, E.; De Angelis, F.; Di Fabrizio, E.; Zaccaria, R. P.; Capiglia, C. Review on Recent Progress of Nanostructured Anode Materials for Li-ion Batteries. *J. Power Sources* **2014**, *257*, 421−443.

(30) Wen, Y. W.; Liu, X.; Duan, X.; Cho, K.; Chen, R.; Shan, B. Theoretical Study of sp^2-sp^3 Hybridized Carbon Network for Li-ion Battery Anode. *J. Phys. Chem. C* **2013**, *117*, 4951−4956.

(31) Liu, J.; Wang, S.; Sun, Q. All-carbon-based Porous Topological Semimetal for Li-ion Battery Anode Material. *Proc. Natl. Acad. Sci. U.S.A.* **2017**, *114*, 651−656.

(32) Fan, D.; Lu, S.; Golov, A. A.; Kabanov, A. A.; Hu, X. D-carbon: *Ab Initio* Study of A Novel Carbon Allotrope. *J. Chem. Phys.* **2018**, *149*, 114702.

(33) Perdew, J. P.; Burke, K.; Ernzerhof, M. Generalized Gradient Approximation Made Simple. *Phys. Rev. Lett.* **1996**, *77*, 3865.

(34) Kresse, G.; Furthmüller, J. Efficient Iterative Schemes for *Ab Initio* Total-energy Calculations Using a Plane-wave Basis Set. *Phys. Rev. B: Condens. Matter Mater. Phys.* **1996**, *54*, 11169.

(35) Heyd, J.; Scuseria, G. E.; Ernzerhof, M. Hybrid Functionals Based On A Screened Coulomb Potential. *J. Chem. Phys.* **2003**, *118*, 8207−8215.

(36) Fan, D.; Lu, S.; Guo, Y.; Hu, X. Novel Bonding Patterns and Optoelectronic Properties of The Two-dimensional SixCy Monolayers. *J. Mater. Chem. C* **2017**, *5*, 3561−3567.

(37) Fan, D.; Lu, S.; Guo, Y.; Hu, X. Two-dimensional Stoichiometric Boron Carbides With Unexpected Chemical Bonding and Promising Electronic Properties. *J. Mater. Chem. C* **2018**, *6*, 1651−1658.

(38) Togo, A.; Tanaka, I. First Principles Phonon Calculations In Materials Science. *Scr. Mater.* **2015**, *108*, 1−5.

(39) Henkelman, G.; Uberuaga, B. P.; Jónsson, H. A Climbing Image Nudged Elastic Band Method for Finding Saddle Points and Minimum Energy Paths. *J. Chem. Phys.* **2000**, *113*, 9901−9904.

DOI: 10.1021/acs.jpcc.9b02034
J. Phys. Chem. C 2019, 123, 15412−15418

(40) Martyna, G. J.; Klein, M. L.; Tuckerman, M. Nosé-Hoover chains: The Canonical Ensemble via Continuous Dynamics. *J. Chem. Phys.* **1992**, *97*, 2635−2643.
(41) Blatov, V. A.; Delgado-Friedrichs, O.; O'Keeffe, M.; Proserpio, D. M. Three-periodic Nets and Tilings: Natural Tilings for Nets. *Acta Crystallogr., Sect. A: Found. Crystallogr.* **2007**, *63*, 418−425.
(42) Blatov, V. A.; Shevchenko, A. P.; Proserpio, D. M. Applied Topological Analysis of Crystal Structures with the Program Package ToposPro. *Cryst. Growth Des.* **2014**, *14*, 3576−3586.
(43) Delgado-Friedrichs, O.; O'Keeffe, M. Identification of and Symmetry Computation for Crystal Nets. *Acta Crystallogr., Sect. A: Found. Crystallogr.* **2003**, *59*, 351−360.
(44) Deringer, V. L.; Csányi, G.; Proserpio, D. M. Extracting Crystal Chemistry from Amorphous Carbon Structures. *ChemPhysChem* **2017**, *18*, 873−877.
(45) Voronin, V. I.; Shekhtman, G. S.; Blatov, V. A. The Natural Tiling Approach to Cation Conductivity in $KAlO_2$ polymorphs. *Acta Crystallogr., Sect. B: Struct. Sci.* **2012**, *68*, 356−363.
(46) Johnston, R. L.; Hoffmann, R. Superdense carbon, C_8: Supercubane or Analog of γ-silicon? *J. Am. Chem. Soc.* **1989**, *111*, 810−819.
(47) Sheng, X.-L.; Yan, Q.-B.; Ye, F.; Zheng, Q.-R.; Su, G. T-carbon: A Novel Carbon Allotrope. *Phys. Rev. Lett.* **2011**, *106*, 155703.
(48) Lu, S.; Wang, Y.; Liu, H.; Miao, M.-s.; Ma, Y. Self-assembled Ultrathin Nanotubes on Diamond (100) Surface. *Nat. Commun.* **2014**, *5*, 3666.
(49) Zhang, J.; Wang, R.; Zhu, X.; Pan, A.; Han, C.; Li, X.; Zhao, D.; Ma, C.; Wang, W.; Su, H.; Niu, C. Pseudo-topotactic Conversion of Carbon Nanotubes to T-carbon Nanowires Under Picosecond Laser Irradiation in Methanol. *Nat. Commun.* **2017**, *8*, 683.
(50) Mouhat, F.; Coudert, F.-X. Necessary and Sufficient Elastic Stability Conditions In Various Crystal Systems. *Phys. Rev. B: Condens. Matter Mater. Phys.* **2014**, *90*, 224104.
(51) Chen, P.; Huang, F.; Yun, S. Characterization of The Condensed Carbon in Detonation Soot. *Carbon* **2003**, *41*, 2093−2099.
(52) Klimeš, J.; Bowler, D. R.; Michaelides, A. Chemical Accuracy for the Van Der Waals Density Functional. *J. Phys.: Condens. Matter* **2010**, *22*, 022201.
(53) Lunell, S.; Stashans, A.; Ojamäe, L.; Lindström, H.; Hagfeldt, A. Li and Na Diffusion in TiO_2 from Quantum Chemical Theory versus Electrochemical Experiment. *J. Am. Chem. Soc.* **1997**, *119*, 7374−7380.
(54) Persson, K.; Hinuma, Y.; Meng, Y. S.; Van der Ven, A.; Ceder, G. Thermodynamic and Kinetic Properties of The Li-graphite System From First-principles Calculations. *Phys. Rev. B: Condens. Matter Mater. Phys.* **2010**, *82*, 125416.
(55) Koudriachova, M.; Harrison, N. M.; de Leeuw, S. W. Open Circuit Voltage Profile for Li-intercalation In Rutile and Anatase From First Principles. *Solid State Ionics* **2002**, *152-153*, 189−194.
(56) Lindström, H.; Södergren, S.; Solbrand, A.; Rensmo, H.; Hjelm, J.; Hagfeldt, A.; Lindquist, S.-E. Li^+ Ion Insertion in TiO2(Anatase). 1. Chronoamperometry on CVD Films and Nanoporous Films. *J. Phys. Chem. B* **1997**, *101*, 7710−7716.
(57) Liu, Y.; Wang, Y. M.; Yakobson, B. I.; Wood, B. C. Assessing Carbon-based Anodes for Lithium-ion Batteries: A Universal Description of Charge-transfer Binding. *Phys. Rev. Lett.* **2014**, *113*, 028304.
(58) Park, C.-M.; Kim, J.-H.; Kim, H.; Sohn, H.-J. Li-alloy Based Anode Materials for Li Secondary Batteries. *Chem. Soc. Rev.* **2010**, *39*, 3115−3141.

DOI: 10.1021/acs.jpcc.9b02034
J. Phys. Chem. C 2019, 123, 15412−15418